Enlargement of Halloysite Clay Nanotube Lumen by Selective Etching of Aluminum Oxide

Elshad Abdullayev, Anupam Joshi, Wenbo Wei, Yafei Zhao, and Yuri Lvov*

Institute for Micromanufacturing, Louisiana Tech University, 911 Hergot Avenue, Ruston, Louisiana 71272, United States

ABSTRACT

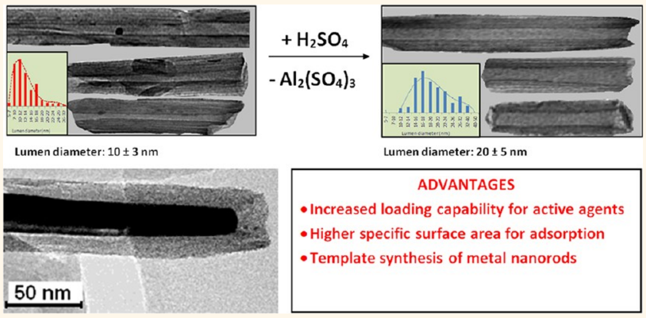

Halloysite clay tubes have 50 nm diameter and chemically different inner and outer walls (inner surface of aluminum oxide and outer surface of silica). Due to this different chemistry, the selective etching of alumina from inside the tube was realized, while preserving their external diameter (lumen diameter changed from 15 to 25 nm). This increases 2–3 times the tube lumen capacity for loading and further sustained release of active chemical agents such as metals, corrosion inhibitors, and drugs. In particular, halloysite loading efficiency for the benzotriazole increased 4 times by selective etching of 60% alumina within the tubes' lumens. Specific surface area of the tubes increased over 6 times, from 40 to 250 m^2/g, upon acid treatment.

KEYWORDS: halloysite · lumen enlargement · alumina etching · encapsulation

Halloysite is a naturally occurring clay mineral with tubular morphology; its external diameter is *ca.* 50 nm, and the inner diameter is 10–15 nm. It has a chemical formula of $Al_2Si_2O_5(OH)_4 \cdot 2H_2O$, which is similar to kaolinite except for the presence of an additional water monolayer between the adjacent clay layers.[1−4] Unlike other tubular materials (such as boron nitride, metal oxide, or carbon nanotubes), halloysite is an abundantly available natural nanomaterial, which makes it attractive for technological applications.[5,6] These clay nanotubes are environmentally friendly and are a perspective biocompatible material for biotechnological research.[7−9] Halloysite belongs to a family of clay minerals and can substitute kaolinite, montmorillonite, and bentonite as additives in material composites.[10] Because of its shape, halloysite material does not require long exfoliation processing due to the absence of the stacked platy sheets (contrary to the platy multilayer clays such as kaolinite). Doping polymers with clay nanotubes remarkably improves the composites' mechanical properties as demonstrated for styrene-butadiene rubber,[11] polyamides,[12] epoxy resin,[13] polypropylene,[14] polymethylmethacrylate,[15] and natural biopolymers.[9] Halloysite application as an additive in polymer composites allows for synergetic strength increase accomplished with controlled sustained release of chemically and biologically active compounds loaded in their lumens. This promises functional polymeric nanocomposites with smart functions (anticorrosion,[16−18] antibacterial,[19] and self-healing[20]).

Many applications of halloysite are conditioned by its lumen size. Typical halloysite lumen volume is *ca.* 10 vol % of the tube, and the pores' enlargement will allow higher amounts of active chemicals loaded with a target capacity of 40–50%. Additionally, more effective anchoring of polymer chains within the tube openings will be possible, which also improves mechanical properties of the clay–polymer composites. We report here an essential increase of halloysite lumen diameter by selective etching of alumina sheets within its lumen, exploiting the different chemistry of the tube's inner and outer surfaces. Recently, data on halloysite acid treatment were presented.[21,22] However, no in-depth kinetic analysis of lumen etching at varying temperatures was performed, which is especially important for nanotube modification with optimal loading and release properties. Reaction conditions (temperature, concentrations of acid and halloysite) were determined, allowing selective etching of the tube inner part and

* Address correspondence to ylvov@latech.edu.

Received for review May 26, 2012 and accepted July 27, 2012.

10.1021/nn302328x

resulting in an increase of the tube lumen diameter from 10 to 15 to 25–30 nm, preserving the clay tubule shape and outer diameter. This drastically enhanced the tube loading efficiency (2–3 times), increasing the inner space available for encapsulation of functional chemical agents, which was demonstrated with silver acetate and anticorrosion benzotriazole loading.

RESULTS AND DISCUSSION

Pure halloysite mineral is white earthy dull matter, as shown in Figure 1a, which is processed to fine powder. Tubular structure of the halloysite with external diameters in the range of 50–70 nm is evident from Figure 1b,c. The length of tubes covers the range of 0.5 to 1.5 μm, and lumen diameter is 10–15 nm. In Figure 1d, one can see a periodic multilayer nature of the halloysite wall as well as views of internal aluminol (Al–OH) and external siloxane (Si–O–Si) surfaces. Periodicity in the individual layer packing was determined with X-ray analysis and was found to be 0.70 $\pm$ 0.02 nm, which corresponds to dehydrated halloysite. Elemental composition of the halloysite is as follows (atomic %): Al, 18.5; Si, 19.1; O, 62.2. Brunauer–Emmett–Teller (BET) surface area of the halloysite sample was 40 $\pm$ 2 $m^2 \cdot g^{-1}$.

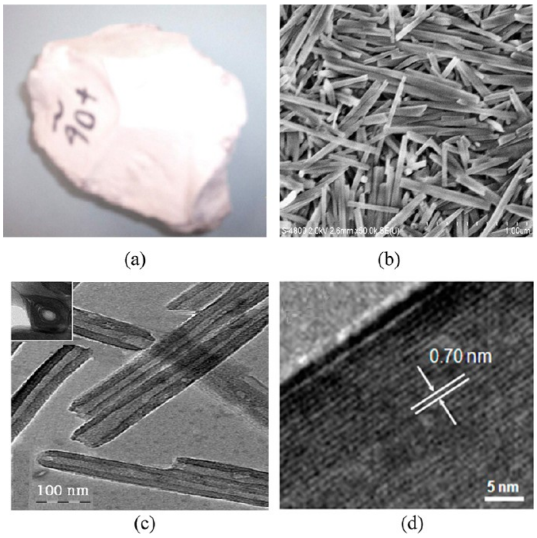
(a) (b) (c) (d)

Figure 1. Halloysite mineral obtained from Dragon Mine Utah, Applied Mineral, Inc., USA (a); SEM of raw powder sample (b); TEM image of tubes with the cross section (inset) and HR-TEM of halloysite multilayer wall (c,d).

Tube Lumen Etching. Sulfuric acid was selected to dissolve alumina sheets from halloysite, following similar works done for kaolinite etching.[23,28] Etching starts by the diffusion of hydrogen ions into halloysite pores, followed by interaction between alumina and hydrogen ions and diffusion of the reaction products outside the pores (Scheme 1). We assume that an opposite phenomenon (*i.e.*, selective silica etching) can be achieved using basic solutions (such as aqueous NaOH). At optimal base concentrations and reaction temperature, one may obtain porous alumina sheets or rods in this case; however, this is out of the scope for this paper.

Halloysite etching was optimized depending on time, temperature, and concentration of the acid. In Figure 2, we present tube morphology depending on percentage of removed alumina. Rodlike structures were preserved even after complete removal of the alumina from halloysites. Some small nanoparticles of *ca.* 20 nm diameter are visible after 50% of the alumina conversion level (Figure 2c–f). These particles are amorphous SiO_2 that are leftover from dealuminated halloysite. Silica nanoparticles are small in the initial stage of the dealumination process and, possibly, cleaned off with the supernatant upon collection of

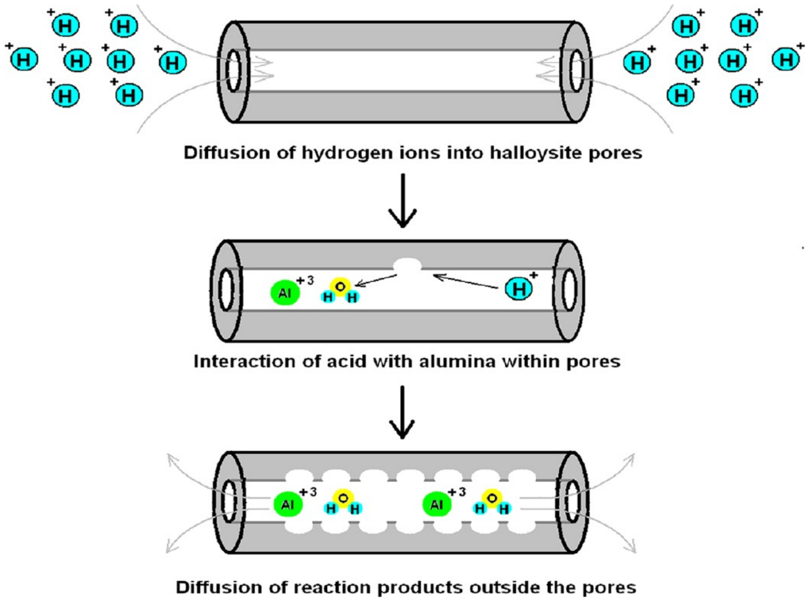

Scheme 1. Acid etching of alumina inner layers from halloysite lumen.

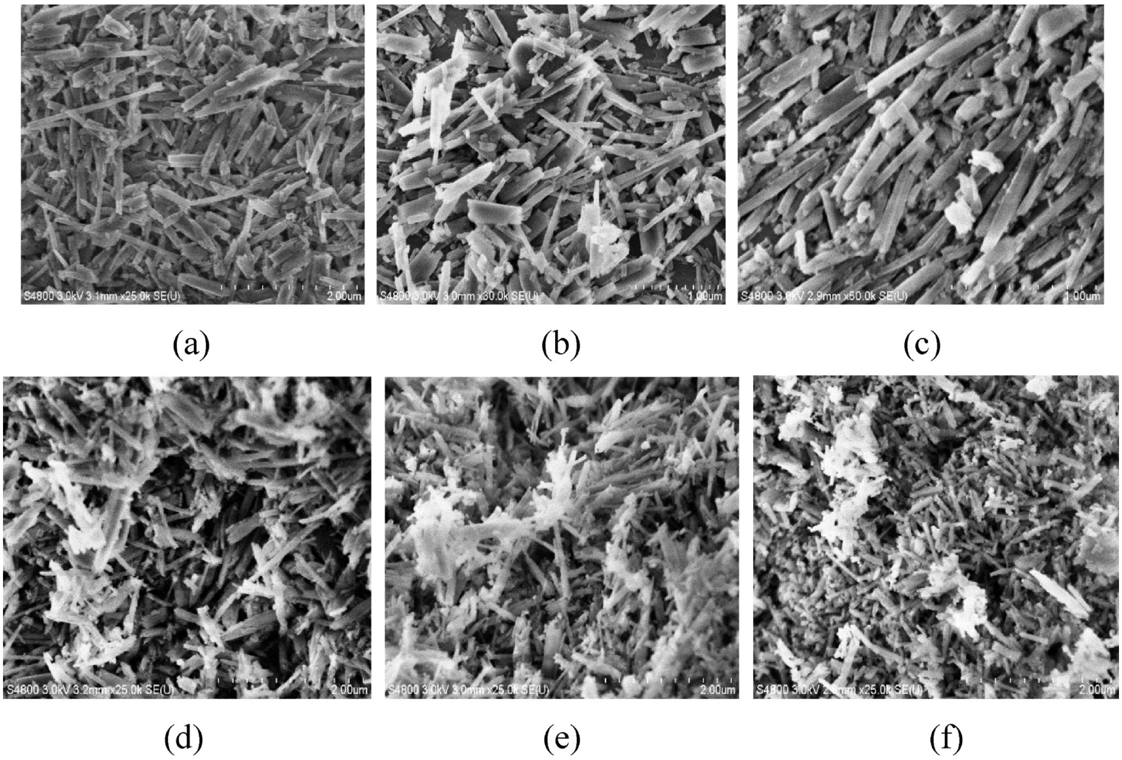

Figure 2. SEM images of halloysite tubes after removal of 20% (a), 40% (b), 50% (c), 75% (d), 88% (e), and 100% (f) aluminum.

the samples by centrifugation. They gradually aggregate and become sufficiently large at 50% of the alumina etching contaminating the sample, as evident from Figure 2d.

In Figure 3, TEM images of halloysite tubes etched at 50 °C are presented. Originally, halloysite had a lumen diameter of 10.0 ± 1.0 nm, and it increased to 21.5 ± 2.0 nm after removal of 20% aluminum and further expanded to 36.3 nm upon 65% dealumination. Enlargement of lumen size was further supported by histograms made with 200 tubes' measurements on TEM images (Figure 3i,j). The external diameters of the tubes remained unchanged, indicating that etching takes place solely in the inner lumen. One can also observe leftover silica nanoparticles of 10–20 nm diameter from dealuminated halloysite walls. These nanoparticles were not observed at a lower level of alumina etching.

The tubes preserved their geometry, while some holes appeared on halloysite walls at the higher level of etching. Halloysite gradually loses its tubular morphology and transforms into porous nanorods upon complete removal of the alumina of the following stages: First, uniform wall thickness is partially lost; second, above 30–40% of the dealumination, tubes with varying wall thicknesses appear; above 50–60% of the alumina removal, pores in the walls start appearing and grow with further etching. Upon complete removal of alumina, tubular morphology is lost and lumen disappears. The final product resembles porous nanorods decorated with nanoparticles. Specific surface area of the tubes increased more than six times upon 80% of the dealumination (~250 m^2/g).

Particle Size Distribution. Dynamic light scattering was used to determine particle size distribution (effective diameter corresponding to the 3D radius of gyration) of the halloysite at various stages of the dealumination (Figure 4). Particles with diameters in the range of 200–300 nm correspond to the individual halloysite tubes.[24] Similar observations were performed in ref 25 using transient light scattering, and dimensions of 315 nm have been ascribed to the individual halloysite tubes. Particles with sizes larger than 400 nm correspond to the agglomerates. Fraction of nonagglomerated tubes increases upon moderate acid treatment. Leftover SiO_2 partially aggregates and forms tiny nanoparticles at the initial etching stage (20–30% dealumination). These nanoparticles are separated from the mixture with centrifugation, yielding pure etched halloysite. At 55% conversion, silica agglomerates to the sizes of 60–100 nm, which was monitored with dynamic light scattering. This is consistent with SEM observations (Figure 3).

FT-IR, ^{29}Si MAS NMR, and XRD Spectral Characterization. Halloysite has several clearly established peaks at 600–3700 cm^{-1} of FT-IR spectral range (Figure 5).[26] Inner OH stretching vibrations of halloysite aluminol groups at 3620 and 3690 cm^{-1} dissapear upon proceeding of the reaction, indicating the removal of alumina layers. Instead a broad peak at 3200–3700 cm^{-1} range with a maxima at 3450 cm^{-1} appears in the FT-IR spectra that correspond to SiO–H vibrations,[27]

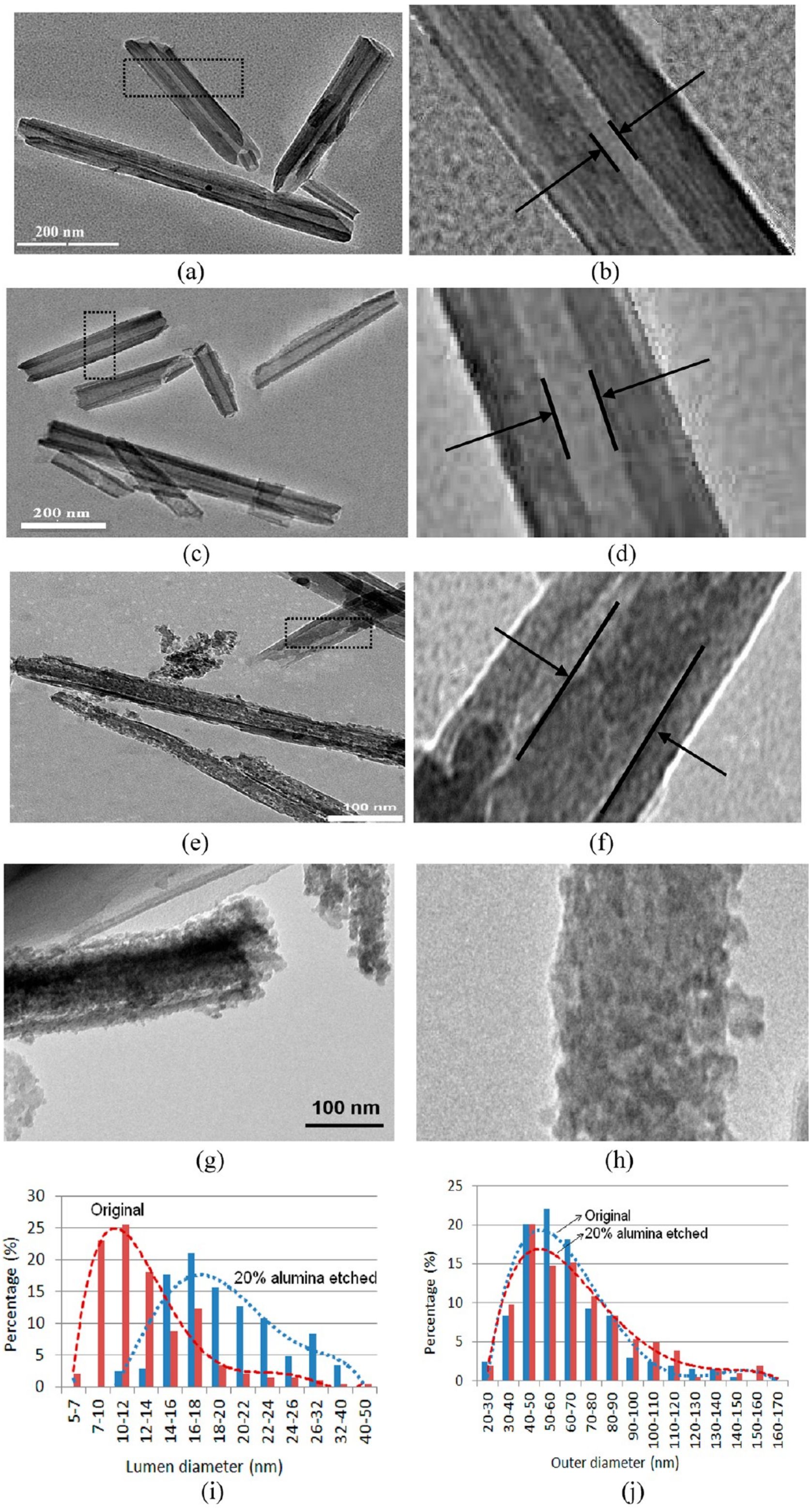

Figure 3. TEM images of pristine halloysite before acid treatment (a,b), after the removal of 20% (c,d), 65% (e,f), and 100% (g,h) of alumina by treatment with H_2SO_4 at 50 °C. External diameters of the tubes are *ca*. 70 nm. Lumen diameters are 9.7, 21.5, and 36.3 ± 2 nm for original, 20 and 65% alumina etched halloysites. Histogram of lumen diameters (i) and external diameters (j) for original and 20% alumina etched halloysite is also shown (based on 200 tubes' measurements).

indicating the formation of silica nanoparticles. Intensity of the in-plane Si–O–Si deformations at 1100 cm^{-1} also increases upon dissolution of the alumina. The signal at 754 cm^{-1} corresponding to the Si–O–Al perpendicular stretching disappears, and the signal corresponding to the symmetric Si–O–Si

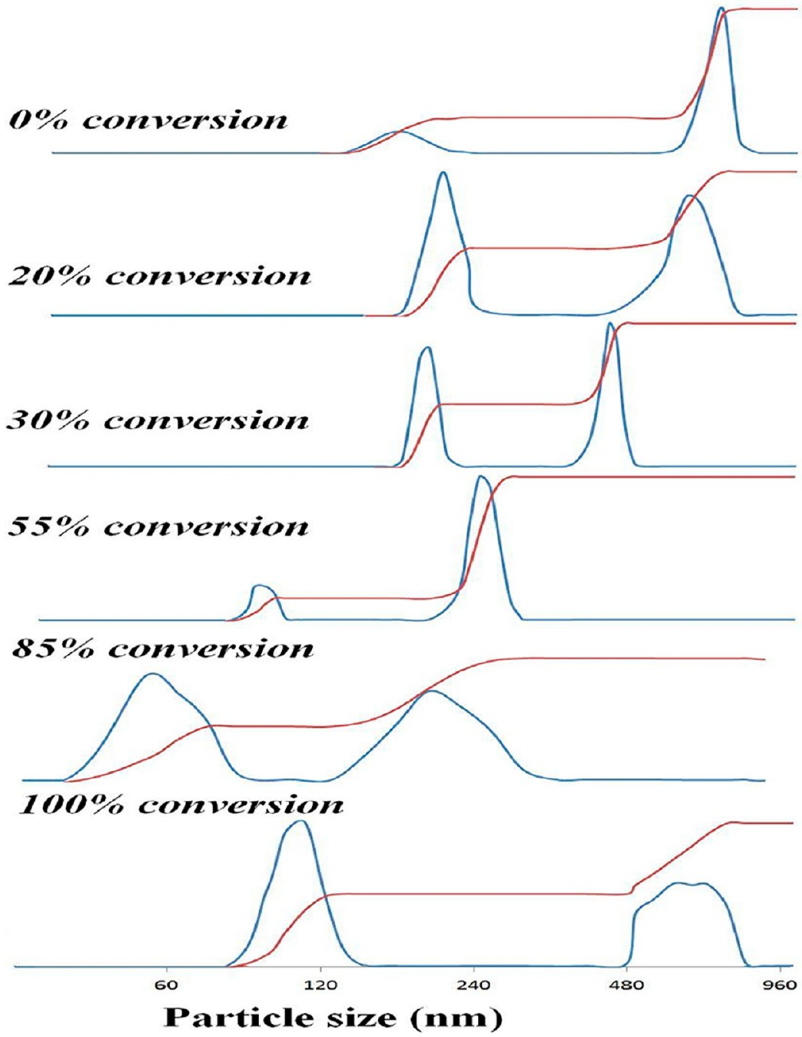

Figure 4. Halloysite particle size distribution at different levels of alumina etching measured by dynamic light scattering.

stretching slightly shifts from 795 to 800 cm^{-1}. In Supporting Information Figure S1, ratios of the FT-IR peaks at 754 and 795–800 cm^{-1} as well as peaks at 1020 and 1100 cm^{-1} are presented. Data clearly indicate that significant changes start appearing in the spectra above 50% of the dealumination. No changes were observed at peak ratios below 40% of the alumina removal, indicating that halloysite structure was essentially unaffected. This can be explained by the removal of silica nanoparticles left over from etched halloysite sheets by the solvent upon centrifugation of the suspension (separation of solid mass from the reaction mixture). This is in aggreement with SEM observations and dynamic light scattering data.

In Figure 6, X-ray diffraction patterns of halloysite powders are shown: d_{001} peak at 7.3 Å corresponds to the multilayer wall packing. Its relative intensity decreases above 40% of the dealumination, indicating the partial loss of the tube wall crystallinity. A 4.5 Å reflection, another characteristic of tubular halloysite,[28] also starts disappearing. No intercalation of sulfuric acid into interlayer space is observed, as the (001) reflection does not shift to lower angles. This indicates that etching of alumina takes place in a layer-by-layer fashion; that is, etching starts from the innermost layer and proceeds toward the outermost layer (contrary to the etching of all layers at the same time, which requires intercalation of sulfuric acid between layers). Absence of silica crystal reflections indicates that most of the silica re-formed is in an amorphous state and very few as quartz microcrystals. A study on kaolinite dealumination reported similar data.[23,29,31,32]

^{29}Si solid-state MAS NMR spectra of the halloysite revealed three types of silicon atoms existing in partially dealuminated samples (Figure 7). The sharp −91.3 ppm signal is assigned to Q^3-type $Si(OSi)_3(OAl_2)$ sites, where each silicon has two second nearest-neighbor octahedral aluminums from the nearby aluminum hydroxide layer of unreacted halloysite. The broader −100 ppm (−96 to −104 ppm) peak is assigned to newly formed Q^3-type silicon sites with one second nearest-neighbor aluminum ($Si(OSi)_3$-(O^+AlH)).[28] The broadest signal at −109 ppm (−100 to −118 ppm) is assigned to newly formed Q^4-type

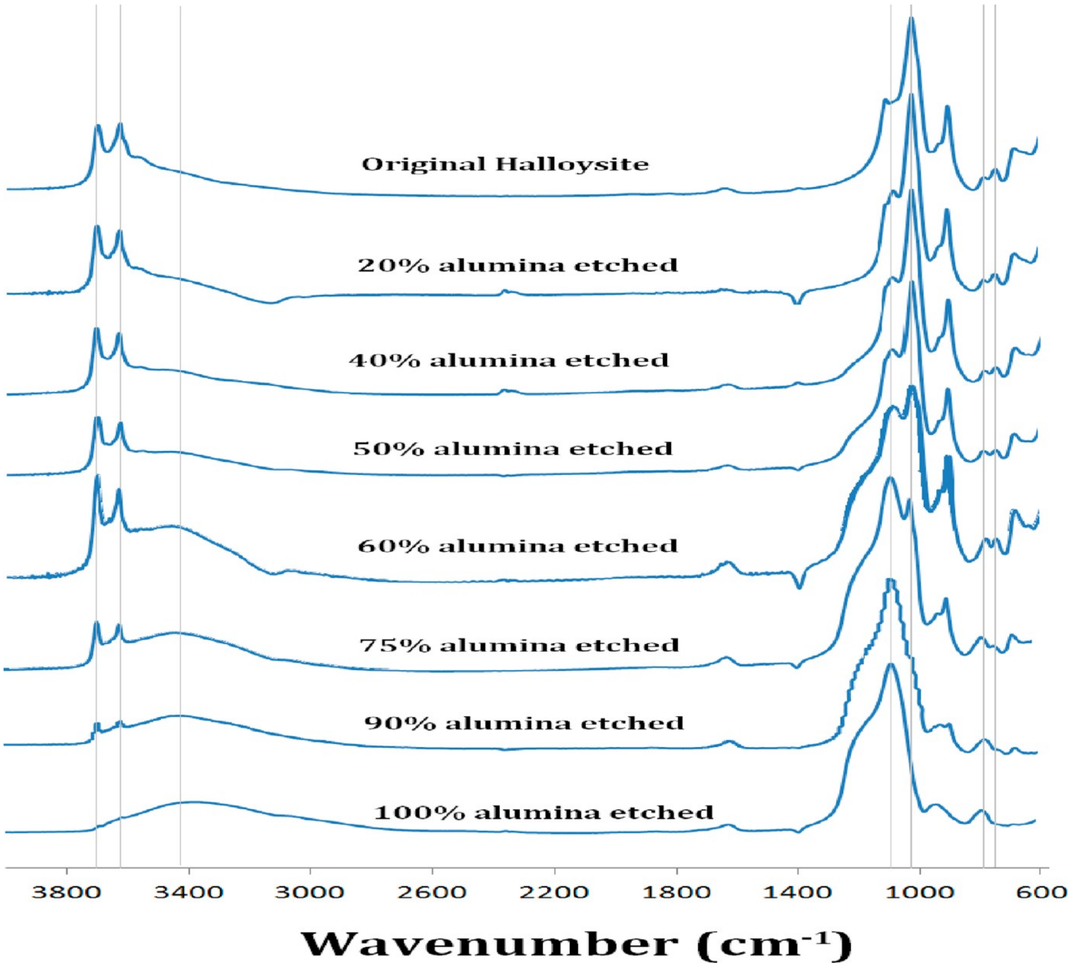

Figure 5. FT-IR spectra of halloysite at different levels of Al_2O_3 conversion.

$Si(OSi)_4$ sites of amorphous silica-like regions in these dealuminated solids.[31] Al solid-state MAS NMR spectra showed that all of the alumina atoms are identical to those in original Al–OH–Al layers of halloysite (Supporting Information Figure S2) with significant alterations observed only at very high level of dealumination (above 90%).

Mechanism of the halloysite layer dealumination was proposed based on NMR observations (Scheme 2), and it suggests hydrolysis of two Si–O–Al and two Al–OH–Al bonds for the release of single Al^{3+} ions. The resulting structure has three different types of silicon atoms (labeled as Q^3_A, Q^3_B, and Q^4_C) and a single type of aluminum. SiO–H bonds are formed as a result of alumina dissolution, which is consistent with FT-IR observations. Nondissolved segments of the halloysite layer preserved its crystalline structure and lattice parameters as was supported by XRD analysis.

Kinetics of Alumina Etching. In Figure 8a, kinetics of the halloysite dealumination at various reaction temperatures are shown. Concentrations of halloysite and sulfuric acid were 10 mg/mL and 1 M, respectively, which correspond to the H_2SO_4/Al ratio of 25:1. Linear profiles indicate that reaction rate corresponds to the pseudo-zeroth order kinetics. Alumina etching rate becomes reasonably high above 50 °C: about 5% of the alumina was dissolved by sulfuric acid at room temperature (18 °C) within 3 days of treatment, while this transformation increased to 40% at 50 °C within the same time frame.

Reaction rate changes with temperature following an Arrhenius equation, which states that certain activation energy E_A is required for the reaction to proceed:

$$v = A^*\exp[-E_A/k_BT] \quad (1)$$

where k_B is the Boltzmann constant and A is the experimental constant. By taking logarithm at both sides, one gets

$$\ln(v) = \ln(A) - \frac{E_A}{k_BT} \quad (2)$$

In Figure 8b, variation of the logarithmic zeroth order reaction rate with reciprocal of the temperature is presented. The reaction rates linearly depend on the temperature up to 70 °C ($1/T = 0.0029\ K^{-1}$). This is the indication that reaction takes place with two different regimes. An activation energy of the processes below 70 °C was calculated from the slope and equal to 68.0 kJ/mol.

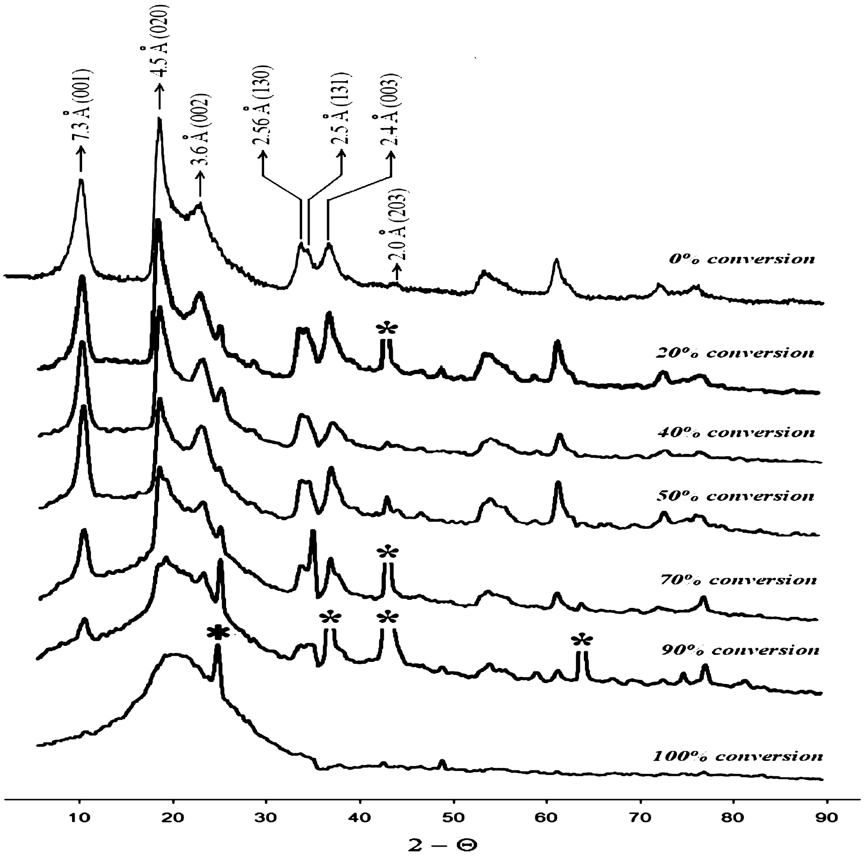

Figure 6. XRD spectra of halloysite at different conversion levels; * aluminum from substrate, * quartz.

This value is typical for the chemical reaction-controlled alumina etching in clay minerals (>42 kJ/mol), while the activation energies for the diffusion-controlled processes through a liquid boundary are less than 10 kJ/mol.[33]

The reaction order in alumina follows zeroth order kinetics below 70 °C and two-thirds order above this temperature (see Supporting Information Figure S3). Two-thirds of reaction order was also reported on aluminum dissolution in kaolinite.[29] In order to analyze reaction order for hydrogen ions, dealumination was conducted by three different concentrations of the sulfuric acid: 0.5, 1.0, and 2.0 M. In Supporting Information, kinetic curves of these processes were shown along with logarithmic curves of linear reaction rate *versus* sulfuric acid concentration (Figures S4 and S5). First-order reaction rate was observed for the halloysite etching at 50 °C, and nearly zeroth order was observed for halloysite etching at 80 °C.

Halloysite nanotubes with 20% dealumination at two regimes, 50 and 80 °C (below and above 70 °C), were analyzed with TEM (Figure 9). Tubes etched at 80 °C had non-uniform lumen enlargement: wider closer to the tube ends and narrower in the middle. Lumen diameter is ~10 nm in the middle section (arrow 2, Figure 9a), while it is over 20 nm close to tube endings (arrows 1 and 3, Figure 9a). This is an indication of the heterogeneous edge-controlled gradient of hydrogen ion reactivity, and it is consistent with data on kaolinite layer etching by hydrogen ions.[30]

On the other hand, halloysite etched temperature lower than 50 °C gives uniform enlargement of the lumen diameter through the all tube length (Figure 9b). In this case, a layer-by-layer stripping of alumosilicate sheets takes place, allowing uniform etching along the lumen.

The influence of acid treatment on halloysite mechanical properties is important considering halloysite applications in polymer composites. In Supporting Information, we give estimations of the relative changes of the halloysite bending stiffness and tensile strength at varying diameters of the inner lumen in the range of 10–40 nm. Both parameters were reduced due to the decrease of the wall thickness (40% decrease for bending stiffness and 60% for tensile strength). Relative change of these parameters per unit weight of the halloysite is more reasonable data since obtaining lower weight polymer additives is as important as the increase in tensile strength. Bending stiffness of halloysite per unit weight actually has increased by *ca.* 58%, while tensile strength remained unchanged.

Enhanced Encapsulation of Chemicals within Halloysite Tubes. Halloysite tubes were proven to be effective

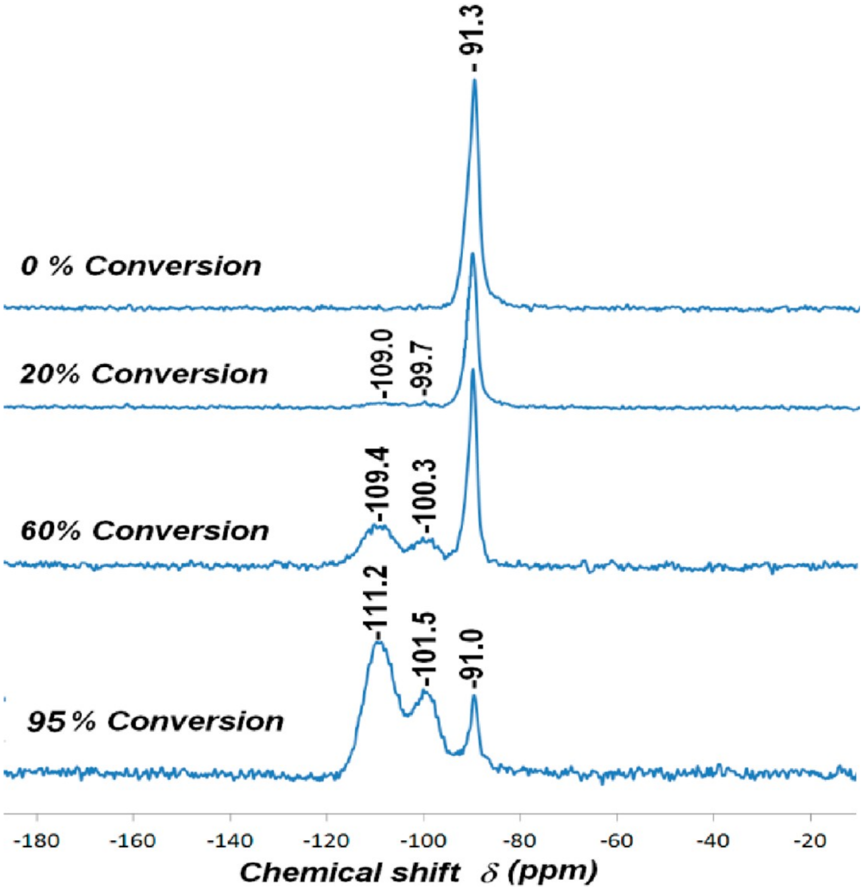

Figure 7. ^{29}Si MAS NMR spectra of halloysite at different levels of alumina dissolution.

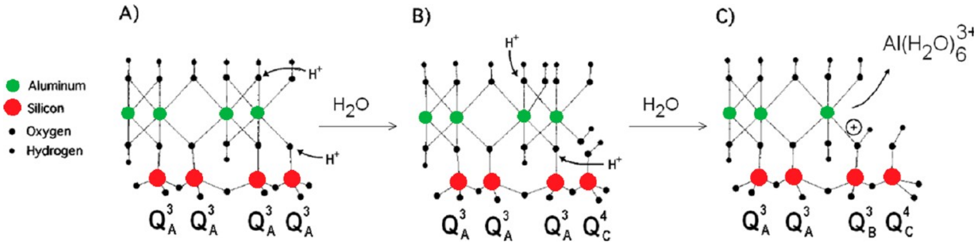

Scheme 2. Schematic of the partially etched halloysite layer with assignments of the silicon nuclei.

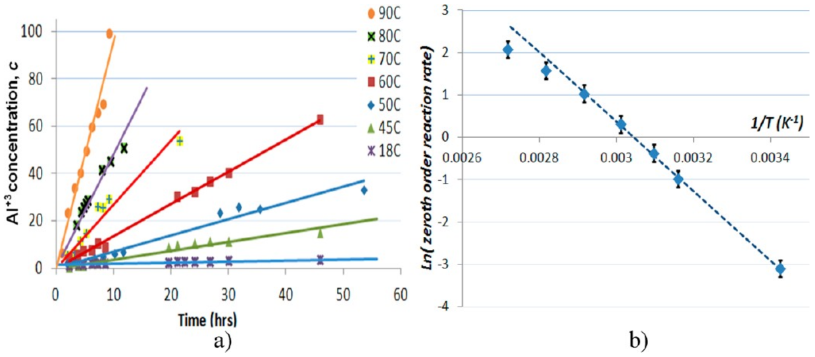

a)

b)

Figure 8. (a) Increase of Al^{3+} concentration in the reaction mixture of halloysites and sulfuric acid *vs* temperature (aluminum concentration was normalized to maximum). (b) Variation of the logarithm of the linear reaction rate on reciprocal of the temperature.

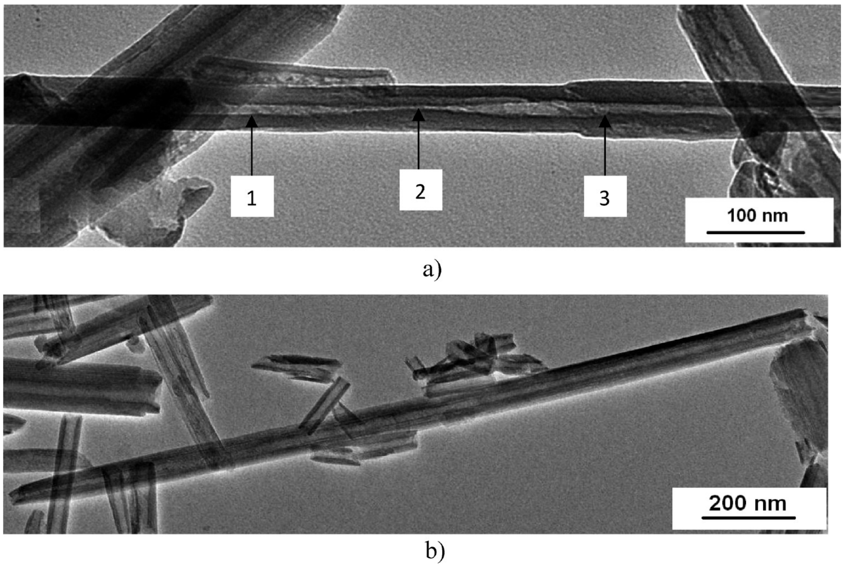

a)

b)

Figure 9. TEM images of the halloysite tubes with 20% alumina removal in two regimes: at 80 °C (a) and 50 °C (b).

nanocontainers for encapsulation of many biologically and chemically active substances such as proteins, drugs, antiseptics, anticorrosive, antifouling, and polymer self-healing agents.[3−9] A general procedure for the halloysite loading is as follows: first, halloysite is mixed with a saturated solution of the compound to be loaded. Solvent has to be not too viscous, provide high solubility of active agent, and allow stable and well-dispersed halloysite colloid (*e.g.*, water, acetone, and ethanol). Once halloysite is added to the solution, the suspension is stirred and sonicated for 15−20 min. Then a beaker is transferred to a vacuum jar, which is then evacuated with a vacuum pump. Slight fizzling of the solution indicates that air is being removed from the tubule lumen. Once the vacuum is broken, active agent enters into the pores and partially crystallizes inside the lumen. This process has to be repeated 3−4 times in order to increase the loading efficiency. With 10 nm lumen diameters, *ca.* 10 wt % loading was typically reached, which is close to the theoretical estimations.[3,4,9]

Following this procedure, silver was loaded into halloysite using aqueous silver acetate solution heated at 300 °C in order to decompose it into metal. As result, tubule lumen was filled with silver, indicating high efficiency of the tube loading, and silver (110) crystalline rod plane was oriented along the lumen (Figure 10). Enlargement of the halloysite lumen allows increasing the silver nanorod diameter to 25 nm. Halloysite walls in the final product can be etched by alkaline solution to yield free-standing nanorods.

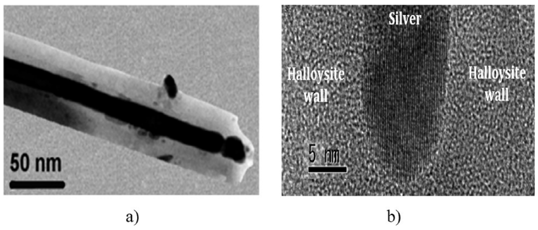

a)

b)

Figure 10. TEM images of silver nanorods within halloysite tubular templates (a) and the magnified image showing silver crystalline planes (b).

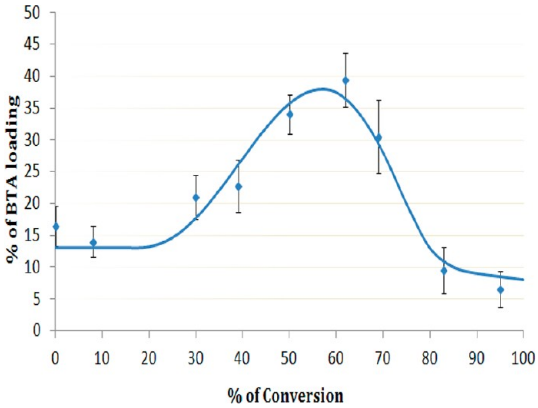

Figure 11. Benzotriazole (BTA) loading efficiency of halloysites treated with sulfuric acid.

Geometrical calculations show that the volume of the tube lumen may increase 3−6 times upon removal of 50−60% of alumina, which was confirmed experimentally with loading of corrosion inhibitor benzotriazole (Figure 11). Halloysite loading efficiency increased 4 times after etching removal of ∼60% of alumina. This is associated with the increase of the both halloysite surface area and inner lumen diameter. Benzotriazole loading drops above 60% alumina etching, and this is due to the formation of multiple holes in the tube walls. Another nondesirable effect of the high (>40%) level etching is formation of silica nanoparticles which are significantly poorer carriers for loaded agents. Therefore, an optimal level of alumina etching is 40−60% depending on application purposes.

CONCLUSIONS

Sulfuric acid treatment provides an efficient method for controllable enlargement of halloysite lumen diameter. Dissolution of alumina sheets starts from inner halloysite layers and, below 70 °C, produces clay nanotubes with uniformly enlarged lumen diameter. Alumina removal from the nanotubes takes place in three steps: diffusion of hydrogen ions into the inner lumen, chemical reaction with alumina on the tube inner wall, and transport of the reaction products out of the lumen. Kinetics study revealed that chemical interaction is the rate-determining step with the activation energy of 68.0 kJ/mol and pseudo-zeroth order below 70 °C.

Above 30−40% of dealumination, significant changes in halloysite morphology were observed: manifesting holes in the halloysite walls, formation of free silica nanoparticles, and, finally, transformation of tubular halloysite into porous silica nanorods. Intensive development of holes in the tube walls at >60% alumina etching decreases their encapsulation efficiency. Loading efficiency of benzotriazole (corrosion inhibitor) was increased 4 times with such etching technique and reached 40 wt %, which is comparable with the conventional polymeric microencapsulation technique.

MATERIALS AND METHODS

Materials. Halloysite was obtained from Applied Minerals, Inc. as a powder and used without further treatment. Sulfuric acid, silver acetate, chromeazurol S, polyvinyl alcohol, urea, acetic acid, and benzotriazole were obtained from Sigma Aldrich.

Characterization. The morphology of halloysite was characterized by scanning electron microscopy (Hitachi S 4800 FE-SEM) at 5−15 kV. Halloysite was coated with 0.5 nm gold by a Cressington sputter coater (208HR) at 20 mA for 1 min. Internal structure of the halloysite was analyzed with transmission electron microscopy (TEM, Zeiss EM 912) at 120 kV. UV−vis spectrophotometer (Agilent 8453) was used to monitor aluminum concentration in the media during etching experiments. Solutions were calibrated relative to pure DI water before each experiment. An X-ray powder diffractometer (Bruker-D8 Discover, Cu Kα radiation) was used for the crystal structure analysis. Halloysite was characterized by a Nicolet Nexus 470 FT-IR spectrometer using KBr pellets in the range of 600−4000 cm^{-1}. In order to improve signal-to-noise ratio, 32 scans were performed with the resolution of 4.0 cm^{-1}. Samples were also characterized with 400 MHz JEOL-Delta NMR spectrometer on ^{29}Si and ^{27}Al nuclei. Poly(dimethylsiloxane) and $AlCl_3$ were used as references for the silicon and aluminum. Appropriate signal-to-noise ratio was achieved after 16 scans. Particle size distribution was obtained by using dynamic light scattering technique (Brookhaven Instruments). Porosity analyses were performed by nitrogen BET adsorption−desorption isotherms (NOVA-2200, Quantochrome Inst). An Eppendorf 5804R centrifuge was used to separate halloysite tubes from colloidal dispersion (7000 rpm for 2 min).

Halloysite Etching by Sulfuric Acid. One gram of halloysite was dispersed in 100 mL of sulfuric acid of 0.5, 1.0 or 2.0 M. Suspension was magnetically stirred on a hot plate at the controlled temperatures between 40 and 90 °C. One milliliter aliquots were taken at certain time intervals and centrifuged to separate halloysites. Supernatant was stored for determination of aluminum sulfate concentration. Processed halloysite was washed 5 times with DI water. The pH of the supernatant from the final washing stage was in the range of 6−7, which is similar to that of pure halloysite suspension. Then sample was dried in the oven at 50 °C. Final sample represented a white solid that was easily crushed into powder using mortar.

Determination of Aluminum Concentration. One hundred milligrams of Chromeazurol S was dissolved in 0.6 mL of concentrated nitric acid solution (50%), and then 50 mL of ethanol and 20 mL of DI water were added. After that, 5 mL of aqueous solution of urea (15 mg/mL) was added and solution was diluted up to 100 mL. This final solution was mixed with acetate buffer, pH 7.1, and polyvinyl alcohol in DI water (40 mg/mL). Concentration of the aluminum was determined by mixing 0.1 mL of the prepared solution with 0.1 mL of the test solution containing Al^{3+} ions. The mixture was kept for 30 min, and concentration was determined by UV reading at 620 nm.

Halloysite Loading with Benzotriazole. To entrap benzotriazole, a 1 mL solution of 20 mg/mL benzotriazole in acetone was mixed with 10 mg of halloysite. A beaker containing this suspension was transferred to a vacuum jar, which was then evacuated using a vacuum pump. Suspension was kept in vacuum until complete evaporation of the solvent. Then excess benzotriazole was washed with 20% ethanol/isooctane and further dried under vacuum. Loading efficiency was calculated from the increase of the halloysite mass.

Halloysite Loading with Silver. Five milligrams of halloysite and 10 mg of silver acetate were added into deionized water, and the suspension was immersed into a vacuum for 30 min; loading of silver acetate was achieved by pulling and breaking vacuum three times. Then, halloysite was washed, precipitated, dried at 80 °C, and heated at 300 °C for 1.5 h to decompose silver acetate into metallic silver.

Conflict of Interest: The authors declare no competing financial interest.

Acknowledgment. The authors acknowledge support by NSF-1029147 and NSF-EPS1003897 grants. Any opinions, findings, and conclusions or recommendations expressed in this report are those of authors and do not necessarily reflect the view of National Science Foundation. The authors would like to thank Atsushi Takahara and Weng On Yah (Kyushu University, Japan) for TEM and solid-state MAS NMR experiments.

Supporting Information Available: FT-IR peak ratios of halloysites at different levels of dealumination. Solid-state ^{27}Al NMR spectra of halloysite samples at various levels of dealumination by sulfuric acid. Kinetic curves of the halloysite dealumination at 80 °C fit to the kinetic models of zeroth, 2/3rd and first-order reaction kinetics. Correlation coefficients of the halloysite dealumination curve at 80 °C fit to the kinetic equations of various orders in aluminum. Kinetic profiles were fit to the equation $Kt = 1 - (1 - X)^{1-n}$, where K is the reaction rate constant, X is halloysite dealumination level at time t, and n is the reaction order in aluminum. Alumina etching curves of halloysites at 50 and 80 °C with sulfuric acid of three different concentrations: 0.5 M (diamonds), 1.0 M (squares), and 2.0 M (triangles); ln(v) *vs* ln(c) curves of the alumina etching profiles, v, reaction rate; c, sulfuric acid concentration. Relative changes of the halloysite bending stiffness and tensile strength. This material is available free of charge *via* the Internet at http://pubs.acs.org.

REFERENCES AND NOTES

1. Joussein, E.; Petit, S.; Churchman, J.; Theng, B.; Righi, D.; Delvaux, B. Halloysite Clay Minerals—A Review. *Clay Miner.* **2005**, *40*, 383–426.

2. Bates, T.; Hilderbrand, F.; Swineford, A. Morphology and Structure of Endellite and Halloysite. *Am. Mineral.* **1950**, *35*, 463–485.
3. Lvov, Y.; Shchukin, D.; Möhwald, H.; Price, R. Clay Nanotubes for Controlled Release of Protective Agents. *ACS Nano* **2008**, *2*, 814–820.
4. Abdullayev, E.; Lvov, Y. Clay Nanotubes for Controlled Release of Protective Agents—A Review. *J. Nanosci. Nanotechnol.* **2011**, *11*, 10007–10026.
5. Lvov, Y.; Price, R.; Gaber, B.; Ichinose, I. Thin Film Nanofabrication *via* Layer-by-Layer Adsorption of Tubule Halloysite, Silica, and Polycations. *Colloids Surf. Eng.* **2002**, *198*, 375–382.
6. Abdullayev, E.; Abbasov, V.; Lvov, Y. Halloysite Clay Nanotubes: Structural Study and Technological Applications. *J. Petrochem. Oil Ref.* **2010**, *23*, 234–246.
7. Kommireddy, D.; Sriram, S.; Lvov, Y.; Mills, D. Layer-by-Layer Assembled Nanoparticle Thin Films—A New Surface Modification Approach for Stem Cell Attachment. *Biomaterials* **2006**, *27*, 4296–4303.
8. Vergaro, V.; Abdullayev, E.; Cingolani, R.; Lvov, Y.; Leporatti, S. Halloysite Clay Nanotubes: Characterization and Biocompatibility Study. *Biomacromolecules* **2010**, *11*, 820–828.
9. Cavallaro, G.; Donato, D.; Lazzara, G.; Milioto, S. Films of Halloysite Nanotubes Sandwiched between Two Layers of Biopolymer: From the Morphology to the Dielectric, Thermal, Transparency, and Wettability Properties. *J. Phys. Chem. C* **2011**, *115*, 20491–20498.
10. Du, M.; Guo, B.; Jia, D. Newly Emerging Applications of Halloysite Nanotubes: A Review. *Polym. Int.* **2010**, *59*, 574–595.
11. Guo, B.; Lei, Y.; Chen, F.; Liu, X.; Du, M.; Jia, D. Styrene-Butadiene Rubber/Halloysite Nanotube Nanocomposites Modified by Metacrylic Acid. *Appl. Surf. Sci.* **2008**, *255*, 7329–7336.
12. Lecouvet, B.; Gutierrez, J.; Sclavons, M.; Bailly, C. Structure−property Relationships in Polyamide 12/Halloysite Nanotube Nanocomposites. *Polym. Degrad. Stab.* **2011**, *96*, 226–235.
13. Ye, Y.; Chen, H.; Wu, J.; Ye, L. High Impact Strength Epoxy Nanocomposites with Natural Nanotubes. *Polymer* **2007**, *48*, 6426–6433.
14. Du, M.; Guo, B.; Liu, M.; Jia, D. Thermal Decomposition and Oxidation Ageing Behaviour of Polypropylene/Halloysite Nanotube Nanocomposites. *Polym. Polym. Comp.* **2007**, *15*, 321–328.
15. Wei, W.; Abdullayev, E.; Hollister, A.; Mills, D.; Lvov, Y. Clay Nanotube/Poly(methyl methacrylate) Bone Cement Composite with Sustained Antibiotic Release. *Macromol. Mater. Eng.* **2012**, *297*, 645–653.
16. Abdullayev, E.; Price, R.; Shchukin, D.; Lvov, Y. Halloysite Tubes as Nanocontainers for Anticorrosion Coating with Benzotriazole. *ACS Appl. Mater. Interfaces* **2009**, *2*, 1437–1442.
17. Shchukin, D. G.; Lamaka, S. V.; Yasakau, K. A.; Zheludkevich, M. L.; Fereira, M. G. S.; Möhwald, H. Active Anticorrosion Coatings with Halloysite Nanocontainers. *J. Phys. Chem. C* **2008**, *112*, 958–964.
18. Abdullayev, E.; Lvov, Y. Clay Nanotubes for Corrosion Inhibitor Encapsulation: Release Control with End Stoppers. *J. Mater. Chem.* **2010**, *20*, 6681–6687.
19. Abdullayev, E.; Sakakibara, K.; Okamoto, K.; Wei, W.; Ariga, K.; Lvov, Y. Natural Tubule Clay Template Synthesis of Silver Nanorods for Antibacterial Composite Coating. *ACS Appl. Mater. Interfaces* **2011**, *3*, 4040–4048.
20. Shchukin, D.; Moehwald, H. Self-Repairing Coating Containing Active Nanoreservoirs. *Small* **2007**, *3*, 926–943.
21. White, R. D.; Bavykin, D. V.; Walsh, F. C. The Stability of Halloysite Nanotubes in Acidic and Alkaline Aqueous Suspensions. *Nanotechnology* **2012**, *23*, 1–10.
22. Zhang, A.; Pan, Li; Zhang, H.; Liu, S.; Ye, Y.; Xia, M.; Chen, X. Effects of Acid Treatment on the Physico-Chemical and Pore Characteristics of Halloysite. *Colloids, Surf. A.* **2012**, *396*, 182–188.
23. Vollet, D. R.; Macedo, J. D.; Mascarenhas, Y. P. Pore Structure Characterization of Kaolin, Metakaolin, and Their Acid-Treated Products Using Small-Angle X-ray Scattering. *Appl. Clay Sci.* **1994**, *8*, 397–404.
24. Abdullayev, E.; Shchukin, D.; Lvov, Y. Halloysite Clay Nanotubes as a Reservoir for Corrosion Inhibitors and Template for Layer-by-Layer Encapsulation. *Polym. Mater. Sci. Eng.* **2008**, *99*, 331–332.
25. Bhanot, M.; Jennings, B. R. Transient Light Scattering from Halloysite Suspensions. *J. Colloid Interface Sci.* **1976**, *56*, 92–99.
26. Yuan, P.; Southon, P. D.; Liu, Z.; Green, M. E. R.; Hook, J. M.; Antill, S. J.; Kepert, C. J. Functionalization of Halloysite Clay Nanotubes by Grafting with γ-Aminopropyltriethoxysilane. *J. Phys. Chem. C* **2008**, *112*, 15742–15751.
27. Vijayalakshmi, U.; Balamurugan, A.; Rajeswari, S. Synthesis and Characterization of Porous Silica Gels for Biomedical Applications. *Trends Biomater. Artif. Organs* **2005**, *18*, 101–105.
28. Tazaki, K. Microbial Formation of a Halloysite-like Mineral. *Clays Clay Miner.* **2005**, *53*, 224–233.
29. Altokka, M R.; Akaln, H.; Melek, N.; Akyalcn, S. Investigation of the Dissolution Kinetics of Meta-Kaolinite in H_2SO_4 Solution. *Ind. Eng. Chem. Res.* **2010**, *49*, 12379–12382.
30. Smith, K. A.; Kirkpatrick, R. J.; Oldfield, E.; Henderson, D. M. High-Resolution Silicon-29 Nuclear Magnetic Resonance Spectroscopic Study of Rock Forming Silicates. *Am. Mineral.* **1983**, *68*, 1206–1215.
31. Fitzgerald, J. J.; Hamza, A. I.; Bronnimann, C. E.; Dec, S. F. Studies of the Solid/Solution "Interfacial" Dealumination of Kaolinite in HCl(aq) Using Solid-State ^{1}H CRAMPS and SP/MAS ^{29}Si NMR Spectroscopy. *J. Am. Chem. Soc.* **1997**, *119*, 7105–7113.
32. Aglietti, E. F.; Porto Lopez, J. M.; Pereira, E. Structural Alterations in Kaolinite by Acid Treatment. *Appl. Clay Sci.* **1988**, *3*, 155–163.
33. Habashi, F. *Principles of Extractive Metallurgy*; Gordon and Breach: New York, 1969; Vol. 1, pp 153−163.